Numerical Modeling for Acoustic Scattering of 3-D Spherical Wavefronts: Implications on Near Source Basin Amplification

Bor-Shouh Huang[1], Ta-Liang Teng[2] and Yeong Tein Yeh[1,3]

ABSTRACT

To understand the complex damage pattern produced by the interaction between a 3-D sedimentary basin and 3-D spherical wavefronts, scattering of seismic waves by 3-D models due to a local point source is investigated by using the Pseudo-Spectrum method. The 3-D wavefields at different time steps are evaluated numerically for a corner diffraction and a sediment-filled basin model. 3-D wavefronts of both models are investigated from snapshots over free surface and vertical cross-sections. Numerical results show that model corners generate strong out-of-plane scattering energy which causes strong seismic energy focusing and defocusing in some specific locations. For an incident wave from a point source below the basin, the sediment-filled basin traps wave energy which propagates inward and focuses near the basin center. This energy extends to the basin bottom with decreasing amplitude. Besides, part of the incident energy is blocked by this basin, resulting in low amplitudes at the surrounding rock sites. This blocking effect is not predicted by the plane wave incidence. Comparisons are made with the results from 2-D models, and they show that the 3-D wavefronts from a point source or from in-plane scattering can be approximated by 2-D models; however, wavefronts from out-of-plane scattering cannot be reproduced.

(Key words: Basin effects, 3-D modeling, Pseudo-spectrum method, Acoustic wave)

1. INTRODUCTION

The recent occurrence of the very damaging Northridge earthquake (M=6.6, January, 17, 1994) in California, with hypocenter 14 km under the San Fernando Valley sedimentary

[1] Institute of Earth Sciences, Academia Sinica P.O. Box 1-55, NanKang, Taipei, Taiwan, R.O.C

[2] Department of Geological Sciences, University of Southern California, Los Angeles, CA, USA, 90089-0740

[3] Institute of Seismology, National Chung Cheng University, Chiayi, Taiwan, R.O.C.

basin, underscore the importance of understanding the interaction of 3-D wavefronts with a 3-D basin. The complexity of the damage pattern in the San Fernando Valley may be, at least in part, a result of the interaction of wavefronts with the basin boundary, which undoubtedly produces localized wavefield focusing, resulting in excessively strong shacking amplification. Prior to the Northridge earthquake, it had been found that data from events nearby the Taiwan SMART-1 array could not be explained by plane wave incidence onto the base of the Langyang sedimentary basin (Abrahamson et al., 1987). Wen et al. (1994) have also found that the strong ground motion response of the 3-D Taipei basin differs by different source approaches.

The phenomenon of scattering of seismic waves in heterogeneous medium has attracted the attention of seismologists and engineers for many years. Because of the complexity of the problem, exact analytic solutions are obtained that are restricted to basins of simple geometries (Trifunac, 1971; Wang and Trifunac, 1974). More general cases must be obtained by numerical methods. In the past two decades, different numerical methods for studying scattering effects have been developed. These include the 2-D Aki-Larner method (Aki and Lamer, 1970) and its 3-D extension (Ohori et al., 1990), the finite difference method (FDM) (Boore, 1972), the finite element method (FEM) (Smith, 1975), the glorified optics method (Hong and Helmberger, 1978), the boundary integral equation method (Dravinski, 1983; Khair et al., 1989; Mossessian and Dravinski, 1990) and the Gaussian bean method (Cerveny et al., 1982). Some hybrid methods which combine the merits of two numerical methods have also been developed (Van den Berg, 1988). Due to the limitations of computational capacity and storage memory of the computer, these methods are usually applied to 2-D cases. Generally, plane waves with different incident angles are employed (Aki and Lamer, 1970; Dravinski, 1983; Van den Berg, 1988). Only a few cases employ a point source or a finite fault rupture (Johnson, 1984; Benz and Smith, 1988; Dong and McMechan, 1991). The rarely developed 3-D extensions of these methods are used to test the accuracy of their methods and only a few computed samples of typical 3-D models are found (Khair et al., 1989; Mossessian and Dravinski, 1990; Ohori et al., 1990). Recently, the finite difference method for 3-D models was applied to more realistic earth models (Frankel and Vidale, 1992; Frankel, 1993; Yomogida and Etgen, 1993). These authors have concentrated on the frequency dependent site responses and time series features on the basin surface. Due to heavy computation, they have generally neglected to analyze the spatial, instantaneous seismic energy distribution inside the basin.

In this paper, the out-of plane scattering of acoustic waves from a local point source in a heterogeneous medium is considered. The present authors have developed a program which bases on the pseudo-spectrum method (PSM) to study acoustic wave propagation in a 3-D medium. The PSM was first developed by computational physicists in the 1970s (Gazdag, 1973; Orszag, 1972). The method is based on the Fourier method to calculate the spatial differentiation of a wave equation. The PSM was applied to explosion seismology in the early 1980's (Gazdag, 1981; Kosloff and Baysal, 1982, Kosloff et al., 1984; Reshef and Kosloff, 1985). It is found that a resolution of ten grid points per smallest period is required for the finite element method or the finite difference method in order to adequately model the wave phenomena, whereas only two grid points are required using the PSM (Fornberg, 1987). The advantages of saving storage memory and getting high frequency resolution are the features of this method. The method, however, is more efficient when used to calculate 3-D problems than 2-D problems (Fornberg, 1987). Supercomputers (the CRAY Y-MP and CRAY 2) were used to execute the numerical code here, its accuracy having been confirmed.

Comparisons with 2-D models are also provided. Numerical results presented here show the effects of the point source excited 3-D wavefield which are not reproduced by a plane wave input motion or 2-D models. Thus, to predict the ground motion inside a 3-D basin excited by an earthquake right below the basin, the consideration of a point source scattering field is necessary.

2. METHOD

2.1 Formulation

The basic equation governing acoustic wave propagation in 3-D medium is as follows:

$$\frac{\partial}{\partial x}(\frac{1}{\rho}\frac{\partial P}{\partial x}) + \frac{\partial}{\partial y}(\frac{1}{\rho}\frac{\partial P}{\partial y}) + \frac{\partial}{\partial z}(\frac{1}{\rho}\frac{\partial P}{\partial z}) = \frac{1}{K}\frac{\partial^2 P}{\partial t^2} + S(x,y,z,t), \qquad (1)$$

where t denotes time, $\rho(x,y,z)$ denotes the density, $K(x,y,z)$ is bulk modules, $P(x,y,z,t)$ denotes the pressure and $S(x,y,z,t)$ denotes the source term (Kosloff and Baysal, 1982). If the density ρ along the x and y axis is constant, the spatial derivative can be simplified and equation (1) can be expressed as:

$$\frac{\partial^2 P}{\partial x^2} + \frac{\partial^2 P}{\partial y^2} + \rho\frac{\partial P}{\partial z}(\frac{1}{\rho}\frac{\partial P}{\partial z}) = \frac{1}{C^2}\frac{\partial^2 P}{\partial t^2} + S'(x,y,z,t), \qquad (2)$$

where $S'(x,y,z,t)$ is the source term expressing the divergence of the pressure, and $C(x,y,z)$ is the velocity of the medium. Equation (1) is more general than equation (2) but involves more numerical calculation for wave propagation. To reduce the numerical computation, for some cases of constant densities along the x and y axes, equation (2) was employed here to compute wave propagation.

2.2 Numerical Solution Technique

In order to numerically solve equation (1) or (2), a discretization in space and time is performed. In this study, the time marching based on the central difference approximation is calculated. From the central difference definition (Wylie, 1975), the physical quantity $\ddot{P}(t)$ is expressed as:

$$\ddot{P}(t) = (P(t - \Delta t) - 2P(t) + P(t + \Delta t))/\Delta t^2, \qquad (3)$$

where double dots express a double differentiation with respect to time. The $\ddot{P}(t)$ deduced from equation (2) can be shown to be:

$$\frac{\partial^2 P}{\partial t^2} = (\frac{\partial^2 P}{\partial x^2} + \frac{\partial^2 P}{\partial y^2} + \rho\frac{\partial P}{\partial z}(\frac{1}{\rho}\frac{\partial P}{\partial z}) - S'(x,y,z,t))C^2. \qquad (4)$$

Hence, the wave field at time $t+\Delta t$ is given from the values at time t and $t-\Delta t$ as follows:

$$P(t + \Delta t) = 2P(t) - P(t - \Delta t) + (\frac{\partial^2 P}{\partial x^2} + \frac{\partial^2 P}{\partial y^2} + \rho \frac{\partial P}{\partial z}(\frac{1}{\rho} \frac{\partial P}{\partial z}) - S')C^2 \Delta t^2 \quad (5)$$

After the spatial Fourier transformation is applied, the spatial derivation can be evaluated by multiplication in the wave number domain. Thus,

$$\frac{\partial P}{\partial x} = \frac{\partial}{\partial x} \frac{1}{N}(\sum_0^{N-1} \hat{P}(k)e^{2\pi i k x/N}) = \frac{1}{N} \sum_0^{N-1} \frac{2\pi i k}{N} \hat{P}(k)e^{2\pi i k x/N}, \quad (6)$$

where

$$\hat{P}(k) = \sum_0^{N-1} P(x)e^{-2\pi i k x/N} \quad (7)$$

is the Fourier transform of $P(x)$. N is the number of data points, and k is the wavenumber. Hence, the left hand side of equation (2) (spatial derivation) can be expressed as:

$$LHS = \frac{-1}{N_x N_y} \sum_0^{N_x-1} \sum_0^{N_y-1} ((\frac{2\pi k_x}{N_x})^2 + (\frac{2\pi k_y}{N_y})^2 \hat{P}(k_x, k_y, z)e^{2\pi i(\frac{k_x x}{N_x} + \frac{k_y y}{N_y})})$$
$$+ \rho \frac{\partial P}{\partial z}(\frac{1}{\rho} \frac{\partial P}{\partial z}) \quad , \quad (8)$$

where $\hat{P}(x_x, y_y, z)$ is the 2-D Fourier transform of the $P(x, y, z)$ with respect to x and y.

2.3 Boundary Conditions

To avoid the wrap-around at the artificial boundaries, some absorbing boundary conditions based on the gradual reduction of wave amplitudes in the vicinity of the boundary (Cerjan et al., 1985; Sochacki et al., 1987) have been proposed. Cerjan et al. (1985) suggested a Gaussian type damper for 2-D acoustic wave cases. Sochacki et al. (1987) proposed 5 different types of dampers (linear, exponent, cubic, exponential and Gaussian) with different dampers for different applications. These suggestions are based on 2-D numerical testing. For efficient absorption of the numerical reflection from the artificial boundaries of the 3-D acoustic wave equation, the present authors have rigorously checked the 5 types of dampers with different absorption coefficients. No damper for 3-D problems have been discussed, before. In this study, a damper for 3-D cases have been rigorously tested for its numerical behavior.

In this study, the free boundary is approximated by including a wide zone with zero velocity above the upper surface of the model to simulate the traction-free condition and to avoid the wraparound propagation waves from the bottom of the model (Reshef et al., 1988 a, b).

2.4 Source Time Function

A time dependent pressure change at a single node is used as a point source. The source time function (Figure 1) is taken as a first directive of a Gaussian function as:

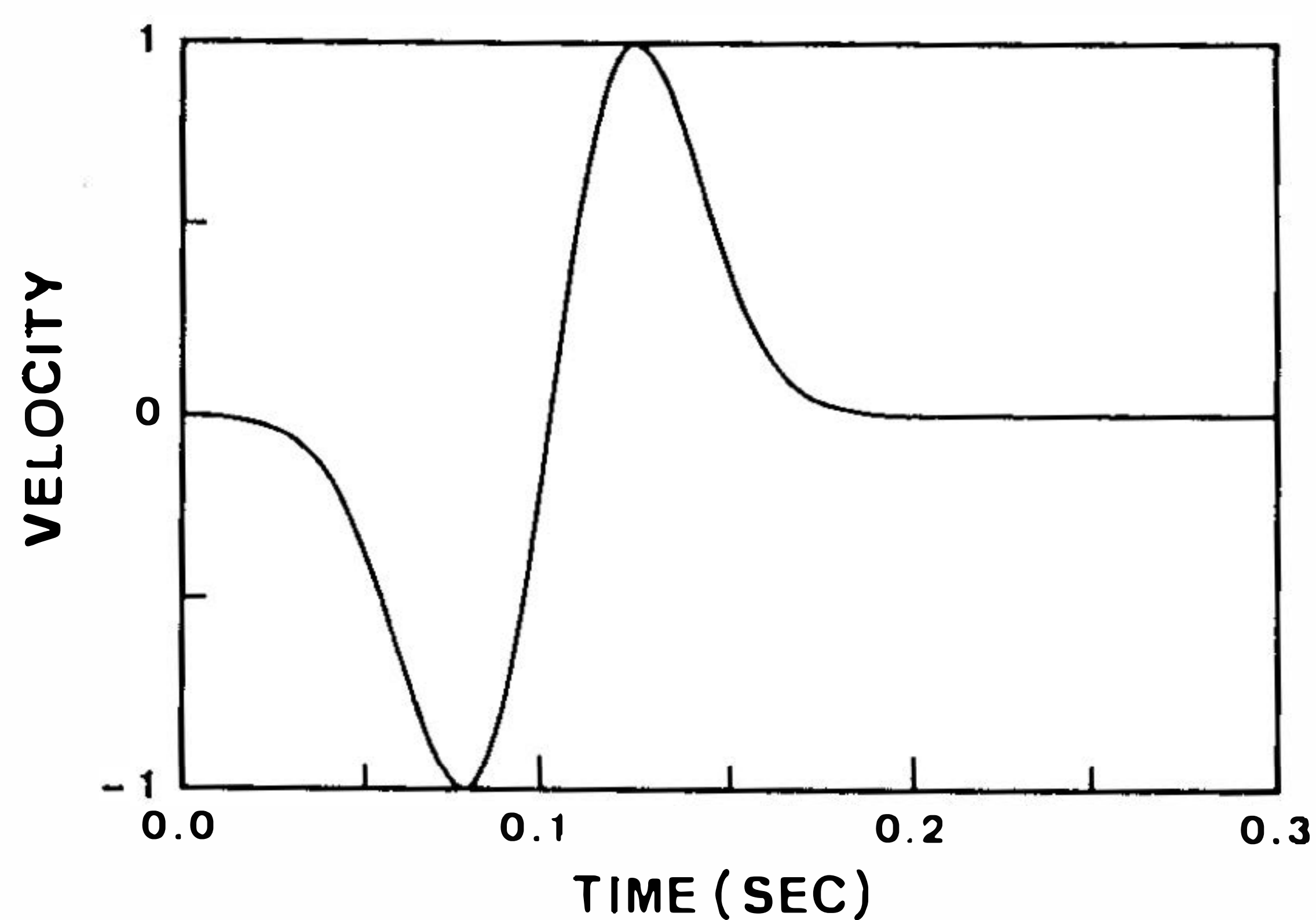$$S(t) = (t - t_0)e^{-\alpha(t-t_0)^2},$$ (9)

Fig. 1. Source distribution time function (Equation 9). Herein, $\alpha=3500$ and $t_0=0.1$ sec are used.

where t_0 is the central time of a wavelet, and α is a coefficient governing the time interval from the negative to positive peak of the function. The Fourier transform spectrum of equation (9) is:

$$F(\omega) = \frac{-i\omega}{2\alpha}(\frac{\pi}{\alpha})^{1/2}e^{\frac{-\omega^2}{4\alpha}}$$ (10)

and is shown in Figure 2. This choice is made as a band-limited spectrum in the frequency domain; however, it is suitable for numerical computation.
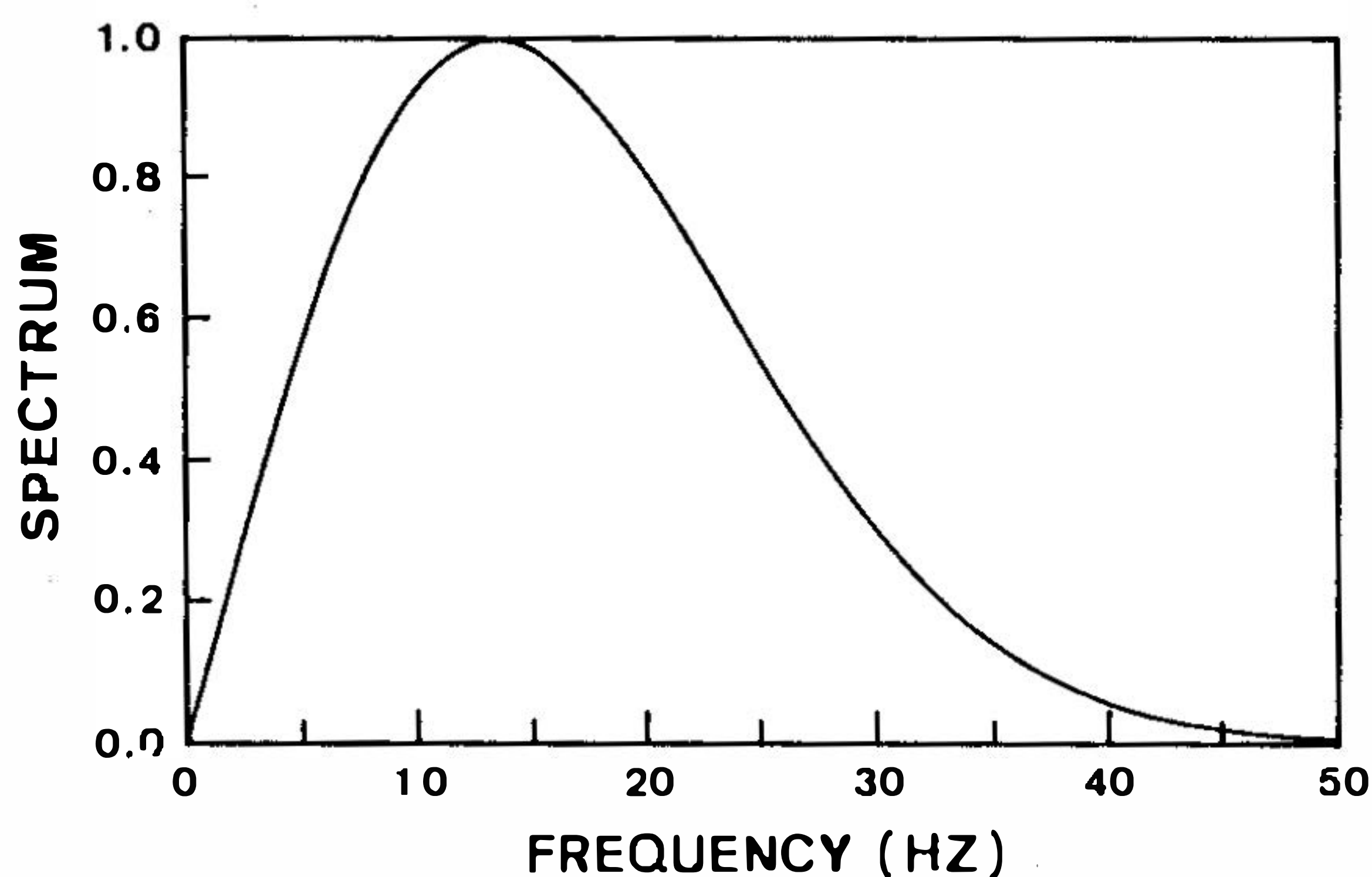

Fig. 2. Normalized source spectrum of Fig. 1.

2.5 Coding and Testing

The 3-D acoustic wave propagation program is developed under the UNIX based operating system. Testing is made on a DEC-3100 workstation, an ETA-10, an IBM-3090 and CRAY series supercomputers, and all have produced stable results. The performance of the PSM is dependent on the speed of the fast Fourier transform (FFT) which is very suitable for parallel and vectorization procedures (Temperton, 1983, 1985). However, the present generation of array and vector processors are quite adequate for computing the FFT. Usually, general scientific computers support high performance 1-D and/or multiple FFT system libraries. With these library routines being used, the computation speed of the code in this study is greatly improved. Different FFT codes from the scientific libraries in different mechanisms are compared. The multiple FFT routine of the CRAY Y-MP has the best performance in executing the code. To check the numerical accuracy of the PSM, the calculated results are compared with other methods (Huang and Yeh, 1991; Huang, 1992). One of them is shown in Figure 3. The comparison of the results of the PSM and the Cagniard-deHoop method (Daudt et al., 1989) illustrates that there are virtually no differences between the resulting waveforms.

3. NUMERICAL RESULTS

3.1 Corner Diffraction Case

The proposed model (see Figure 4) includes two media with a low velocity and low density (1.5 km/sec and 2.2 g/cm^3, respectively) cubic corner inside an otherwise homogeneous medium with a uniform velocity of 2.6 km/sec and a density of 2.4 g/cm^3. The model size, which is represented by grid numbers, is set at 128×128×128 with space intervals (Δx, Δy and Δz) of 200 m. The low velocity corner has dimensions of 1.3 km both on the x and y axes and 1.1 km on the z axis. Over the free surface (z=1.66 km), a fictitious layer has been placed with a velocity of 0.01 km/sec on top of the model which numerically simulates a free boundary. An explosive type point source is located at 0.1 km above the corner with coordinates of x=1.3 km, y=1.3 km and z=1.2 km. The source time function is shown as equation (9) with α=3500 and t_0=0.05 sec. The computed 3-D wavefield snapshots at time intervals of 0.40 and 0.44 seconds after the explosion are shown in Figure 4, where the snapshots of the 3-D wavefields as equal amplitude surface have been displayed as shown. In order to show the reflection inside the direct wavefront, the wavefields with a y coordinate of less than 0.8 km are made transparent in Figure 4. Some propagation phases are clearly seen in the snapshots. Two selected vertical wavefield cross-sections at time 0.44 sec are shown in Figure 5. In the cross-section of y=0.8 km (Figure 5 (a)), which includes the low velocity corner and does not include the source, the phases defined in Figure 4 are clearly seen. It is also evident that, due to the source location above the corner, the transmitted waves from the upper corner surface (phase E_z in Figure 4(b)) are stronger than those from the vertical corner surface (phase E_x in Figure 4(b)). Both E_z and E_x have crossed each other causing a transmitted curved wavefront (phase F in Figure 5 (a)) behind. In the vertical cross-section of y=1.6 km (Figure 5 (b)), which is in the homogeneous medium behind the low velocity corner, the diffraction from the upper surface of the low velocity corner and its free surface reflection (phases C and D) are smaller in amplitude than the direct and reflection waves (phases A and B). The strength of phase D decreases in amplitude farther away from
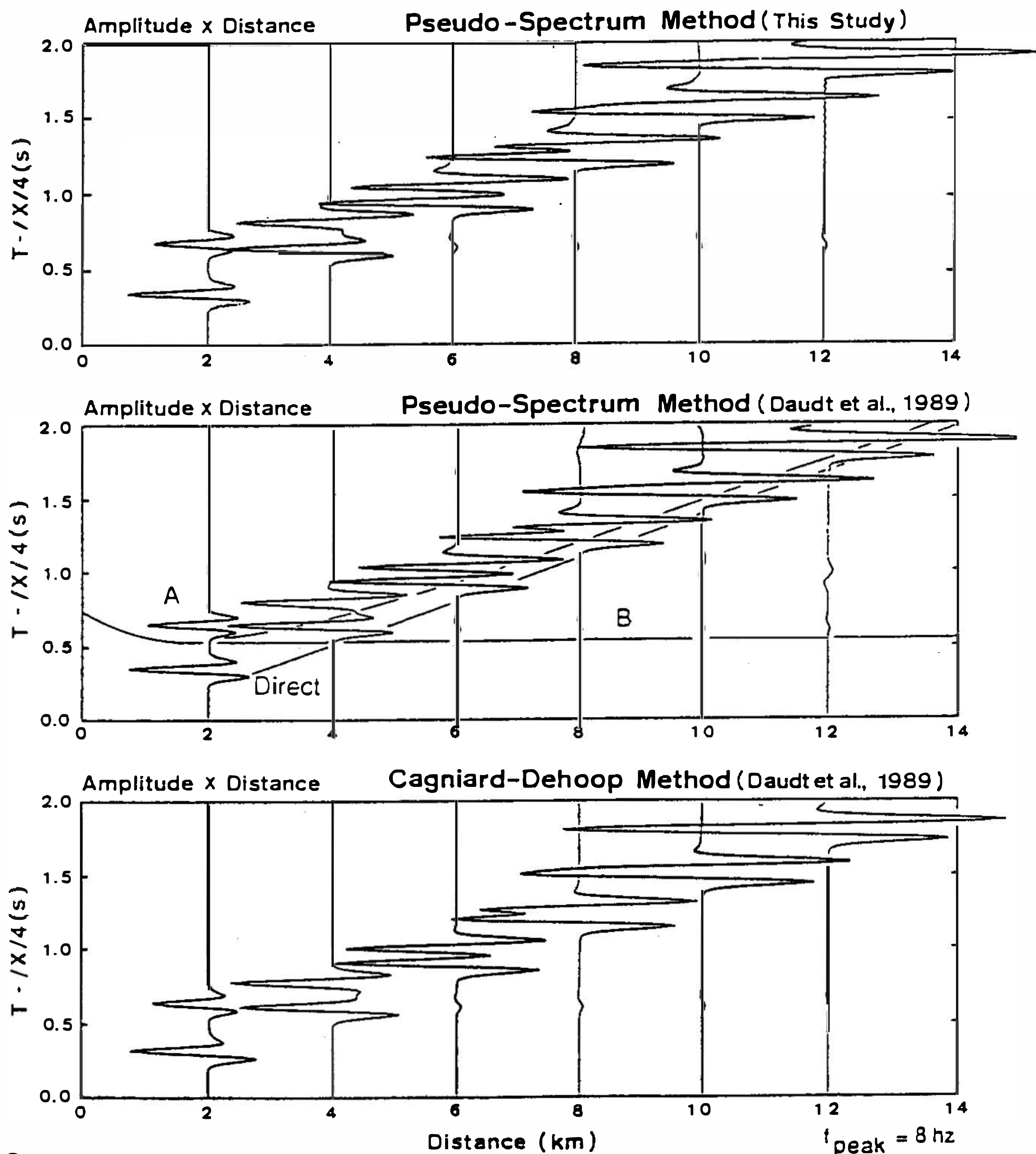
Fig. 3. Computed seismograms using the pseudo-spectrum method and Cagniard-deHoop method for a model with single interface. The velocities for the upper and lower layers are 2.5 km/sec and 4.0 km/sec, respectively. The source function is an 8.0 Hz peak frequency Ricker wavelet. The locations of observation used in this simulation follow the model proposed by Daudt *et al.* (1989).

the diffraction corner. The horizontal wavefield cross-sections of $z=0.8$ km and $z=1.6$ km are shown in Figure 6. In the cross-section of Figure 6 (a), the major energy transmitted into the low velocity region is from phase E_z. The two phases (E_x and E_y in Figure 6 (a)) which enter this cross-section horizontally from both vertical corner surfaces are identified. The same as in the vertical cross-section, both E_x and E_y in Figure 6(a) have crossed each other causing a curved wavefront behind (phase F). The velocity ratio between the two media measured from the 2-D cross-section (assumed to be the source located in this cross-section) is nearly 0.4 which is different from that for the real velocity ratio of both media (0.576). The difference comes from the source location of the 3-D model far away from this cross-section
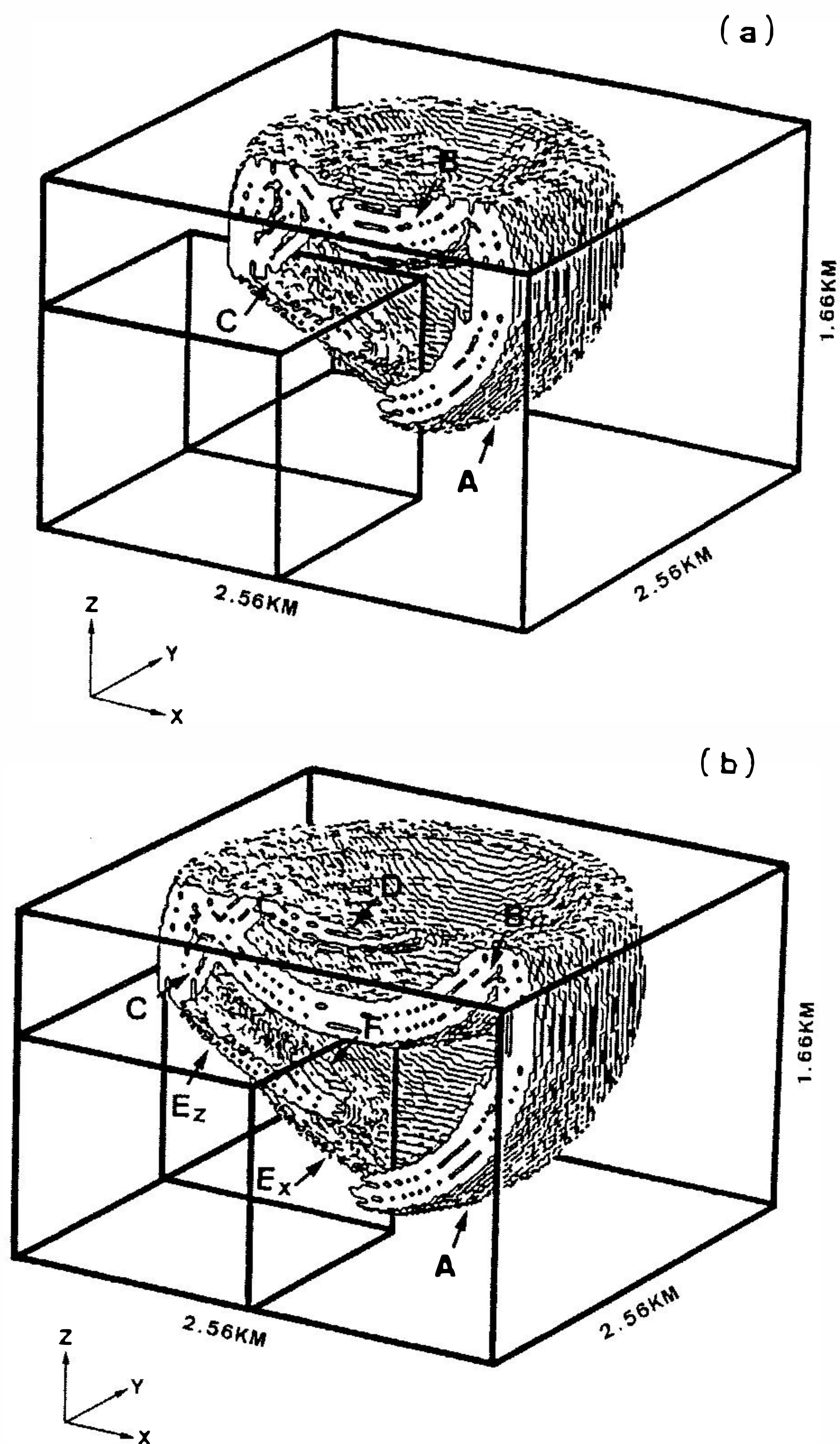
Fig. 4. 3-D wavefront snapshots for a corner diffraction model at different time steps. (a) t=0.40 sec, (b) t=0.44 sec. A: direct wave, B: free surface reflection, C: corner upper surface reflection, D: C-phase's free surface reflection, E_x: the transmission from the vertical corner surface of $x=1.3$ km and E_z: the transmission wave from the upper corner surface of $z=1.1$ km. F: transmission wave (see text). The source is located at 0.1 km above the tip of the high velocity corner.

of 0.4 km. The apparent velocity ratio on both media is less than the real velocity ratio in this vertical profile. The stratigraphic wavefronts of phases E_z, E_x and E_y are examined from the individual 2-D cross-sections of the 3-D wavefields. E_z has the shape of a quarter cone with its axis in the z direction, while both E_x and E_y have the shapes of a quarter cone with their axes in the x and y directions, respectively. The wavefront of phase F is found to be a quarter spherical shape. The reflection waves (phases C and D in Figure 4) are found on the cross-section above the low velocity corner (Figure 6(b)).
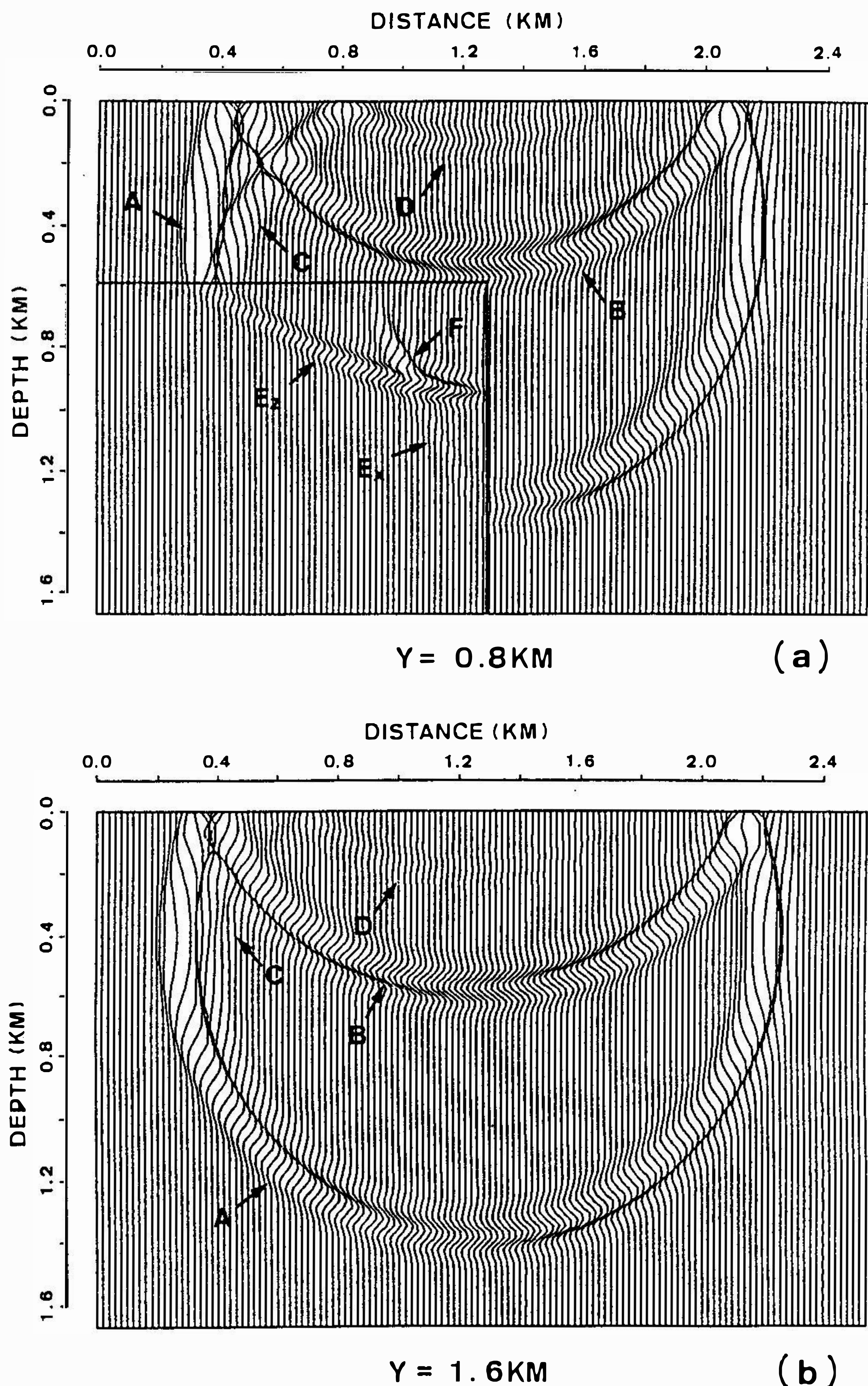
DISTANCE (KM)

Y = 0.8KM   (a)

DISTANCE (KM)

Y = 1.6KM   (b)

Fig. 5. Vertical cross-sections of Fig. 4(b) at (a) y=0.8 km and (b) y=1.6 km. The vertical axis is defined as the depth from free surface. The definitions of the symbols are the same as those in Fig. 4(b). The amplitude of the spatial wavefield of each panel is normalized individually and the same as the other cross-sections in this study.

3.2 Sediment-filled Basin Case

The 3-D basin model used for the numerical experiments is shown in Figure 7. The model parameters and source time function are the same as the corner diffraction case. The model includes a quarter ellipsoid sharp sediment-filled basin with a velocity of 2.0 km/sec
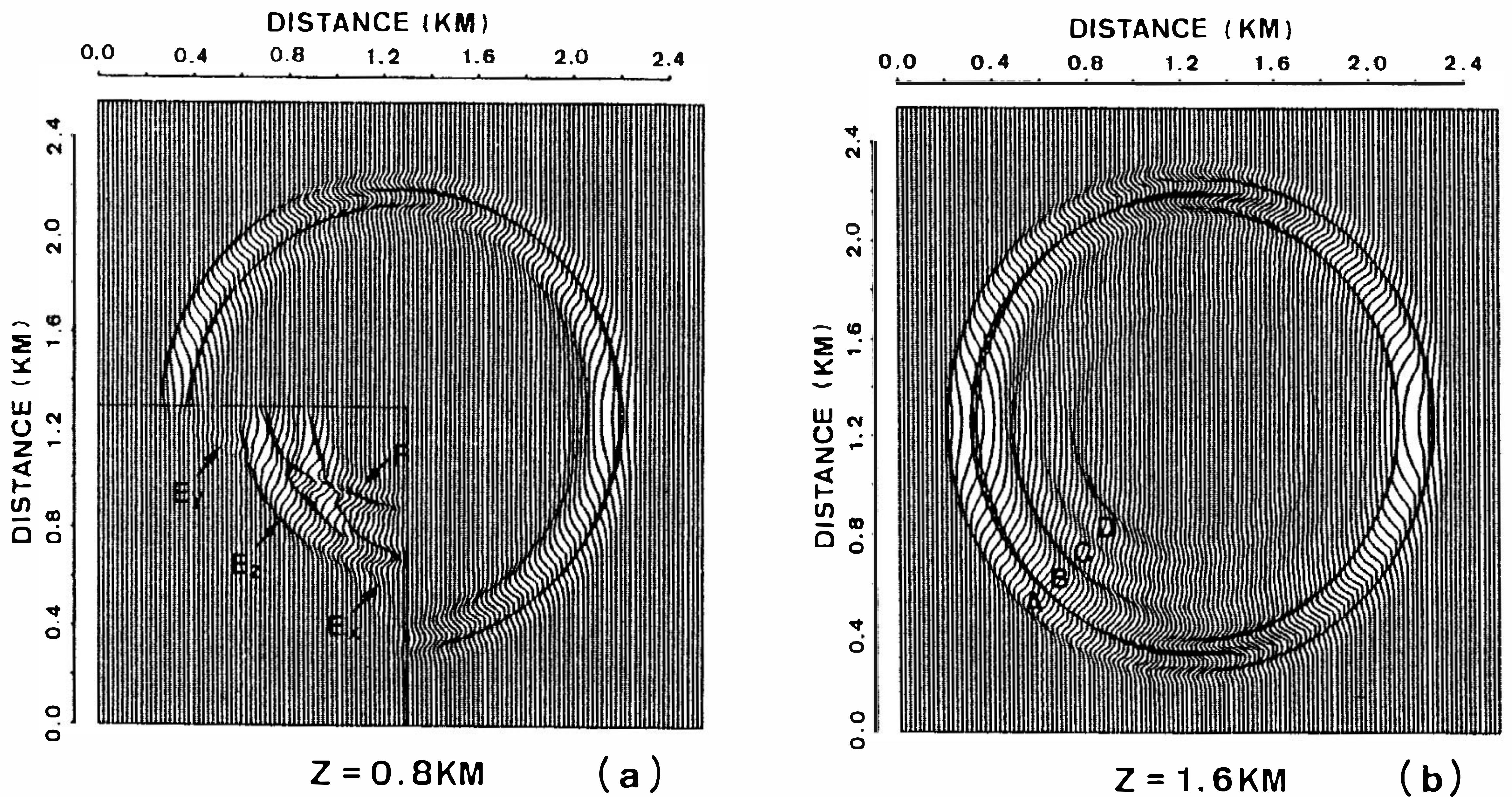
Fig. 6. Horizontal cross-sections of Fig.s 4(b) at (a) z=0.8 km and (b) z=1.6 km. E_y is the transmission wave from the vertical corner surface of y=1.3 km. The definitions of other symbols are the same as those in Fig. 4(b).
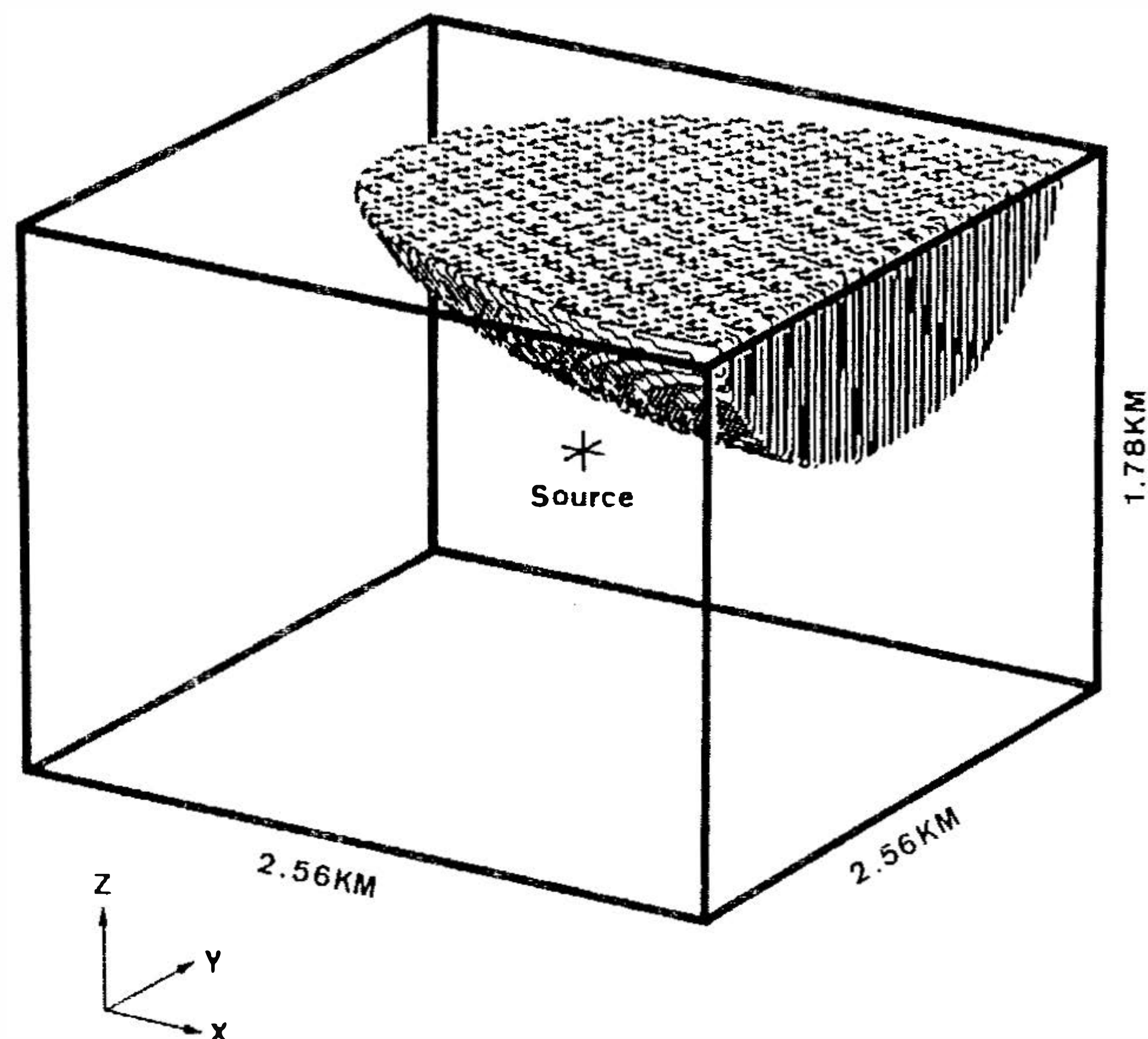

Fig. 7. A 3-D sediment-filled basin model used to calculate acoustic wave propagation effects. The shadow zone expresses the basin with a velocity of 2.0 km/sec and a density of 2.3 g/cm^3 with a good contrast to the bedrock of velocity (2.6 km/sec) and density (2.4 g/cm^3). The source is located at x=1.3 km, y=1.3 km and below the basin with z=0.88 km.
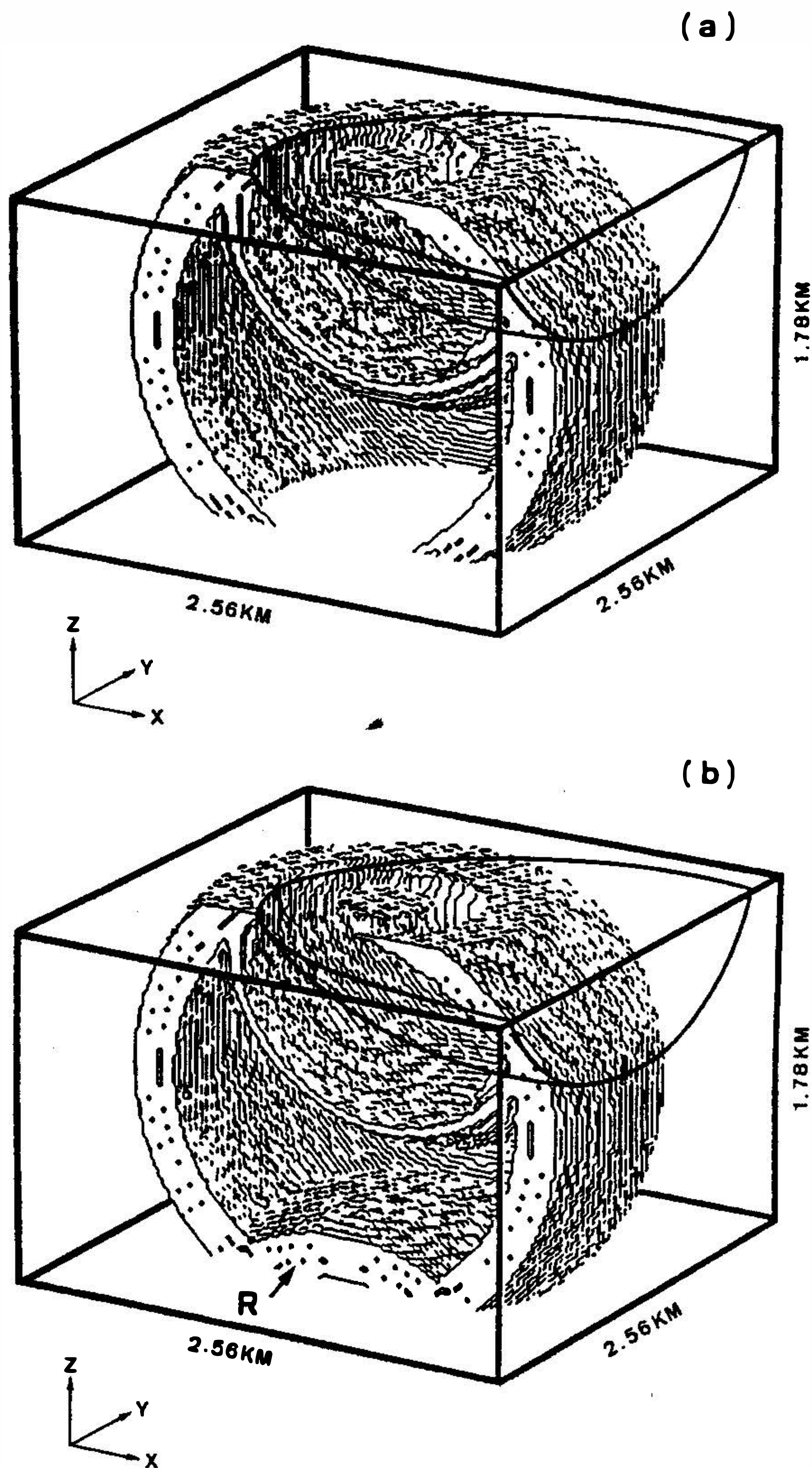
Fig. 8. Seismic snapshots (t=0.48 sec) display a comparison between (a) with and (b) without an absorption boundary of the experimental basin model (Fig. 7). The solid lines express the outline of the basin. The wavefields with a coordinate y less than 0.8 km are transparent. R: the artificial boundary reflection phase.

and a density of 2.3 g/cm^3 with a good contrast to the bedrock of velocity (2.6 km/sec) and density (2.4 g/cm^3). The ellipsoid has a 3:2:1 ratio of long (x), intermediate (y) and short (z) axes. The source used in this study is a point source just below the basin (as shown in Figure 7) to simulate a near-basin earthquake. The strong artificial boundary reflection is found in the propagating wavefield as shown in Figure 8. It was found that the Gaussian damper best reduced the artificial reflections. The Gaussian damper is expressed in the form of exp($-ad^2$), where a is the absorption coefficient, and d is the distance (expressed in grid points) from the inner boundary of the absorbing layer. In this study, many absorption parameters for

study, many absorption parameters for the 3-D acoustic wave equation have been tested, and it has been found that an absorption coefficient of $a=0.025$ coupled with an absorbing distance of 17 grid points had reduced wraparounds to an acceptable level as shown in Figure 8(a). Comparative results without absorption boundaries are shown in Figure 8(b). No optimum values of absorption parameters are obtained in the testing procedure here. Larger values of d coupling with smaller values of a of the absorption parameters produce better absorption of artificial reflection. For computation efficiency, a special test is required for the particular problem of interest.

The 3-D wavefront snapshots of the experimental model at later time steps than in Figure 8 are shown in Figure 9. The wavefront of the direct wave (phase A), the basin bottom reflection (phase B) and the transmitted wave and its reflected phase from the free surface (phase C) are observed. The special wavefront (phase D) of the acoustic wave trapped on the basin is clearly seen in Figure 9(b). The plane snapshots of the free surface wavefield at different time steps are plotted in Figure 10. Two interesting features are observed in these snapshots. First, from the blocking of this low velocity basin, the incident wavefront is disconnected on both sides of the basin boundary, and the incident wave decreases its amplitude as it approaches the basin boundary. Tracing the wavefront in time, there are two regions of the basin boundary that give lower peak amplitude than the incident wave (Figure 10). Second, the basin traps energy that propagates inward and focuses energy near the center of the basin of this model. Two vertical cross-sections of 3-D snapshots are shown in Figure 11. The trapped wavefield is clearly seen in the cross-sections and on different time steps. Phase (D), as trapped energy in the basin, extends to the basin bottom with decreasing amplitude from top to bottom. As phase (D) hits the basin boundary, a strong reflection is generated that keeps most of the wave energy within the basin, much the same as a wave excited in an ellipsoidal swimming pool. Reflections from all parts of the basin boundary approach each other forming regions of wave focusing in a manner dependent on the nature of the basin boundary. Two subsurface horizontal snapshots with different elevations are shown in Figure 12. The wavefield inside the basin includes the horizontal propagation trapped waves (Figure 12(a)), while outside (Figure 12(b)) the basin, no trapped waves are found.

3.3 Cross-section Related to 2-D Cases

The 2-D models, with an infinite extension of the third dimension of the 3-D experimental models, are selected to compute the wavefield for comparison with the 3-D model. Two cross-sections related to Figure 5 are chosen, and the computed wavefield of the corner diffraction model (not shown) is very similar to its related 3-D cross-section (Figure 5(a)); however, the diffraction phases C and D of Figure 5 (b) are missing in the 2-D half-space model (not shown). The computed wavefield of the 2-D model related to Figure 6 (a) is shown in Figure 13 (a). In this case, the source is located exactly at the corner point. The wavefield of Figure 13 (a) is very different from that of the related 3-D cross-section (Figure 6 (a)). The amplitude of the wavefield in the low velocity corner is stronger than that in the other region; besides, phases E_z, E_x and E_y are not found. Phases E_x and E_y can be reproduced by shifting the source slightly away from the corner as shown in Figure 13 (b). Phase E_z cannot be reproduced because it propagates into this cross-section vertically, and the out of plane wavefield cannot be simulated by a 2-D model. The same reason explains why phases B, C and D of Figure 6 (b) cannot be simulated by a full-space 2-D model.
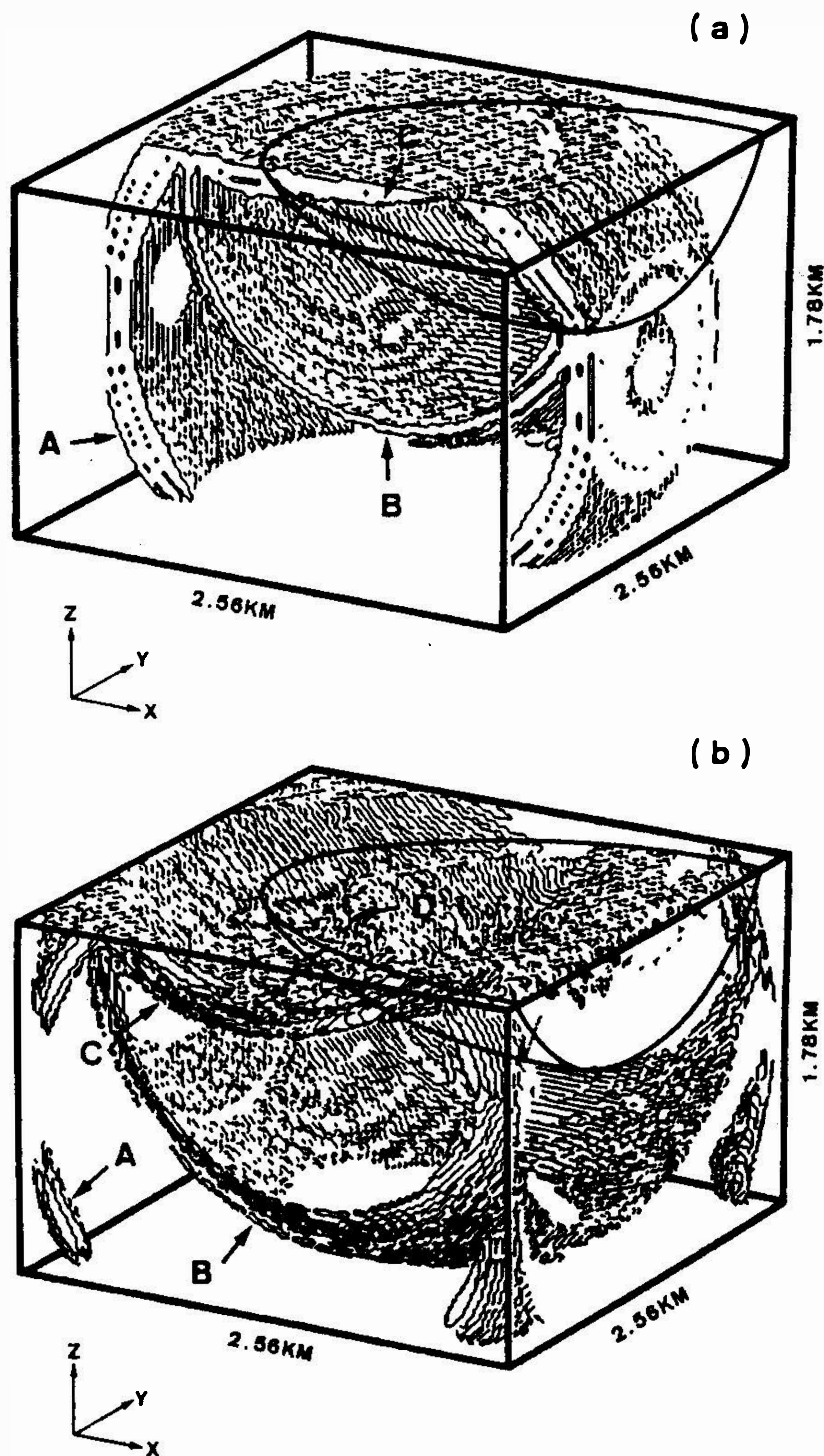
Fig. 9. 3-D wavefront snapshots for the experimental basin model (Fig. 7) at different time steps. (a) t=0.56 sec, and (b) t=0.72 sec. A: wavefront of the direction wave. B: basin bottom reflection. C: transmitted then reflected from free surface. D: wavefront of seismic wave trapped on the basin. The solid lines show the outline of the basin. The wavefield of Fig. 9(a) with a coordinate *y* less than 0.8 km is transparent.

Figures 14(a) and (b) represent snapshots of the 2-D model which is the vertical cross-section of the 3-D basin model (Figure 7) at *y*=1.2 km, and they are used to compare Figures 11(a) and (b). Their corresponding wavefronts are very similar. The slight difference between them is due to the difference in source location. The source for Figure 11(a) or (b) is out of the 3-D cross-section plane by 0.1 km (*y*=1.3 km). Figures 14(c) and (d) give snapshots of the 2-D model as a vertical cross-section of the 3-D basin model at *x*=1.3 km, a plane which includes the point source. Figures 14(c) and (d) can be selected for comparison with
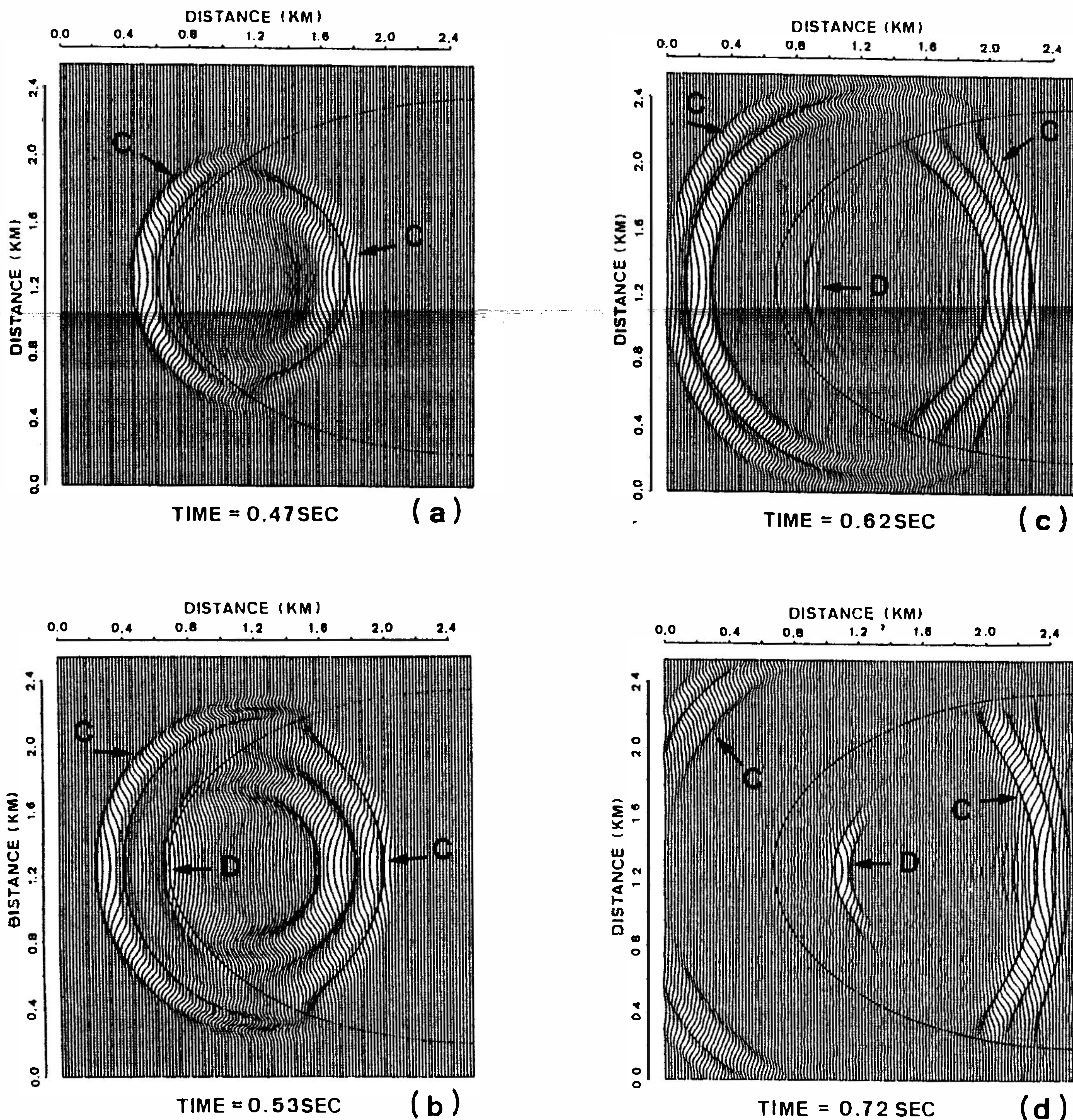
Fig. 10. Horizontal snapshots of the free surface (z=1.78 km) for the experimental basin model (Fig. 7) at different time steps. The solid lines show the boundary of the basin and bedrock. Phase indexes refer to Fig. 9.

Figures 11 (c) and (d). In Figures 11 (c) and (d), the 3-D snapshot cross-sections are located at x=1.6 km, and the source is far away from the plane (Figure 7). Due to the lateral heterogeneity in the x direction, even though the shapes of the basin for both cross-sections are similar, the spatial distribution of these wavefronts are very different. This shows the limitation of using 2-D models for a 3-D interpretation. Besides, no corresponding 2-D models can be used to approximate the wavefield snapshots for the free surface or for any horizontal cross-sections produced by the 3-D model (Figure 12).
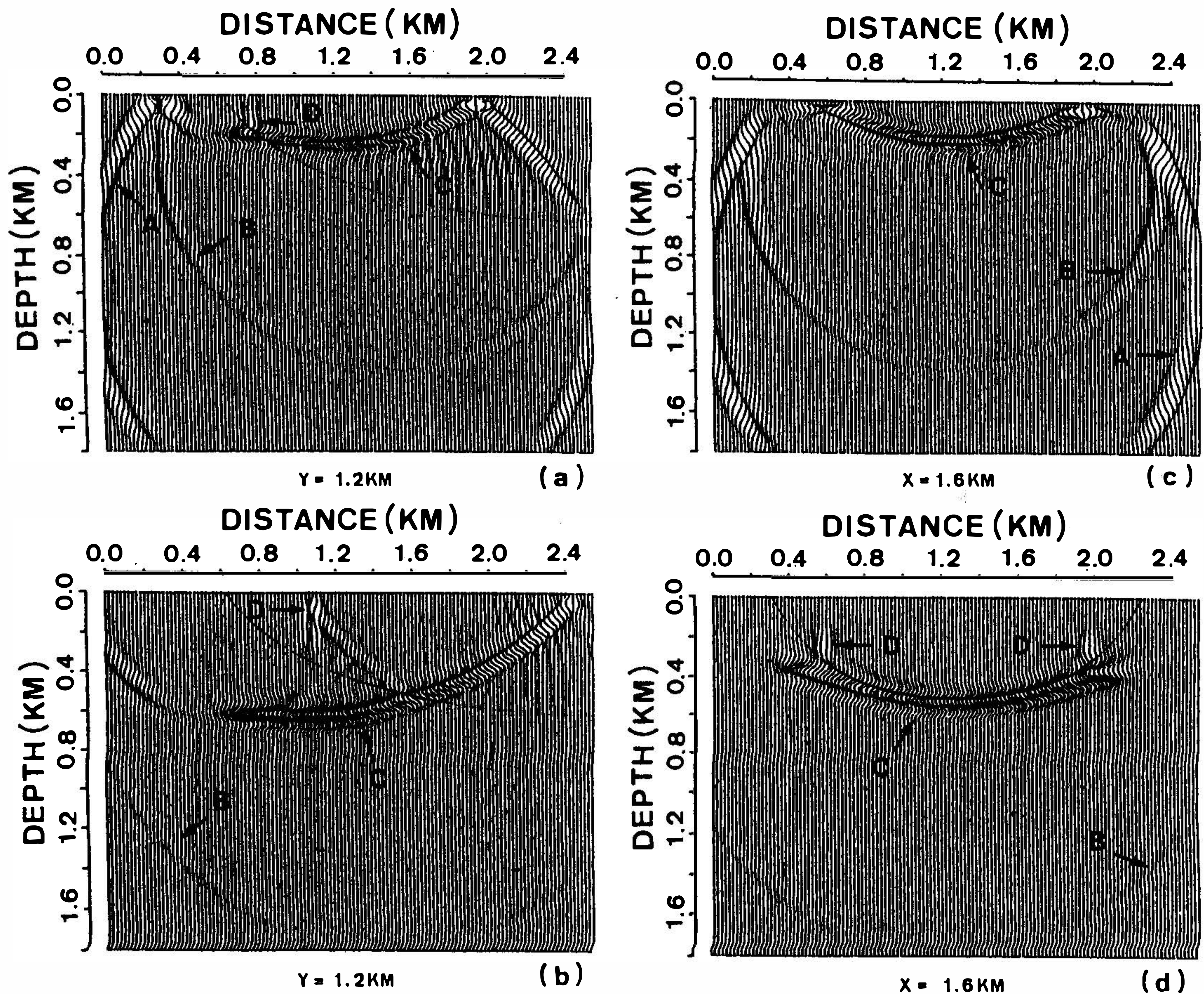
Fig. 11. Vertical snapshots at different cross-sections and time steps of the experimental basin model (Fig. 7). (a) t=0.56 sec, and (b) t=0.72 sec for the cross-sections at y=1.2 km, and (c) t=0.56 sec and (d) t=0.72 sec for the cross-section at x=1.6 km. The solid lines show the boundary of the basin and bedrock. The vertical axis is defined as the depth from the free surface. Phase indexes refer to Fig. 9.

4. DISCUSSION

In this study, through 3-D numerical computations, it may be understood that excessively strong ground motions can be generated by the localized wavefield focusing effect as a result of the interaction of a 3-D basin with incoming 3-D spherical wavefronts. Until recently, there were only a few cases for 3-D basin response computations which mainly involved plane wave incidence. Finite fault and point source effects are less often discussed. Generally, discussion on site effects is separated from that on source effects, and it usually neglects the wave scattering effects induced by distance variations from source to basin. However, when the source is close to the basin, it has been found that, even in such simple models as those used in this study, the wavefields are strongly disturbed by the configurations of the 3-D
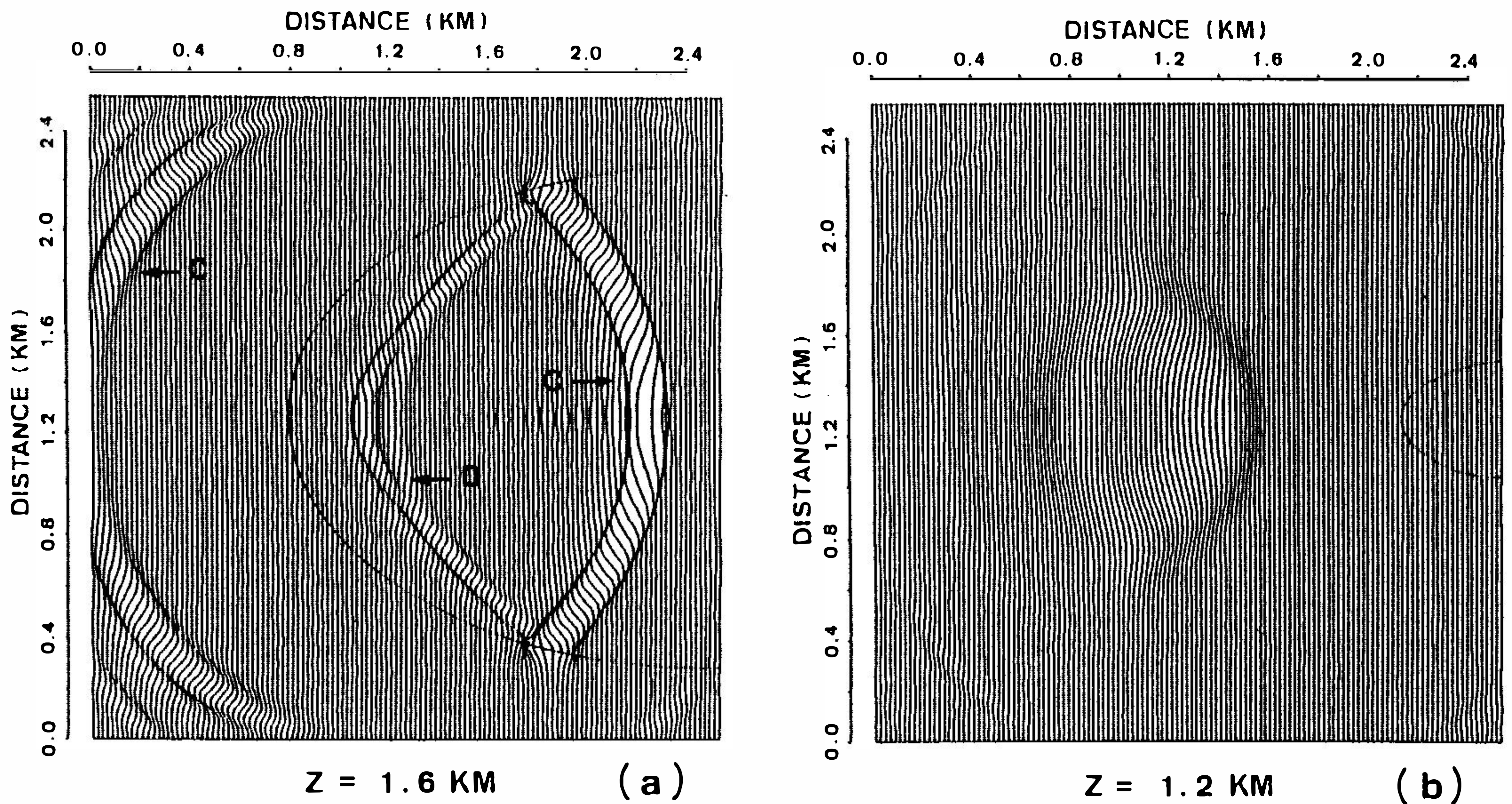
Fig. 12. Horizontal snapshots (t=0.72 sec) at different depths for the,experimental basin model (Fig. 7). The solid lines show the boundary of the basin and bedrock. Phase indexes refer to Fig. 9.
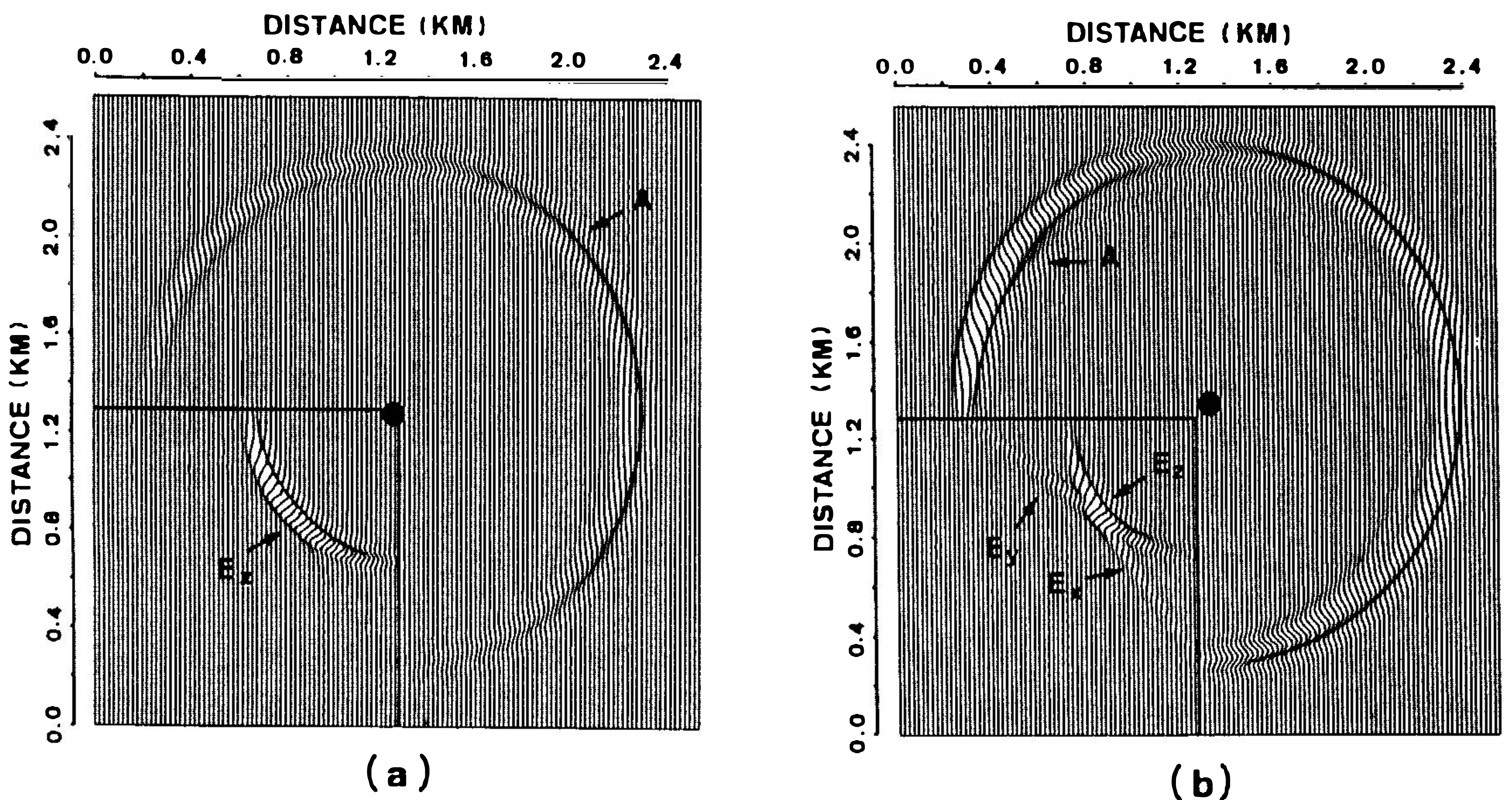

Fig. 13. 2-D wavefield snapshots which relate to cross-sections of the 3-D corner diffraction snapshot (Fig. 6(a)) on t=0.44 sec with (a) source located at x=1.3 km, y=1.3 km, and (b) source located at x=1.36 km, y=1.36 km. Solid circle represents the position of source of the 2-D model. Phase indexes refer to Fig. 6.
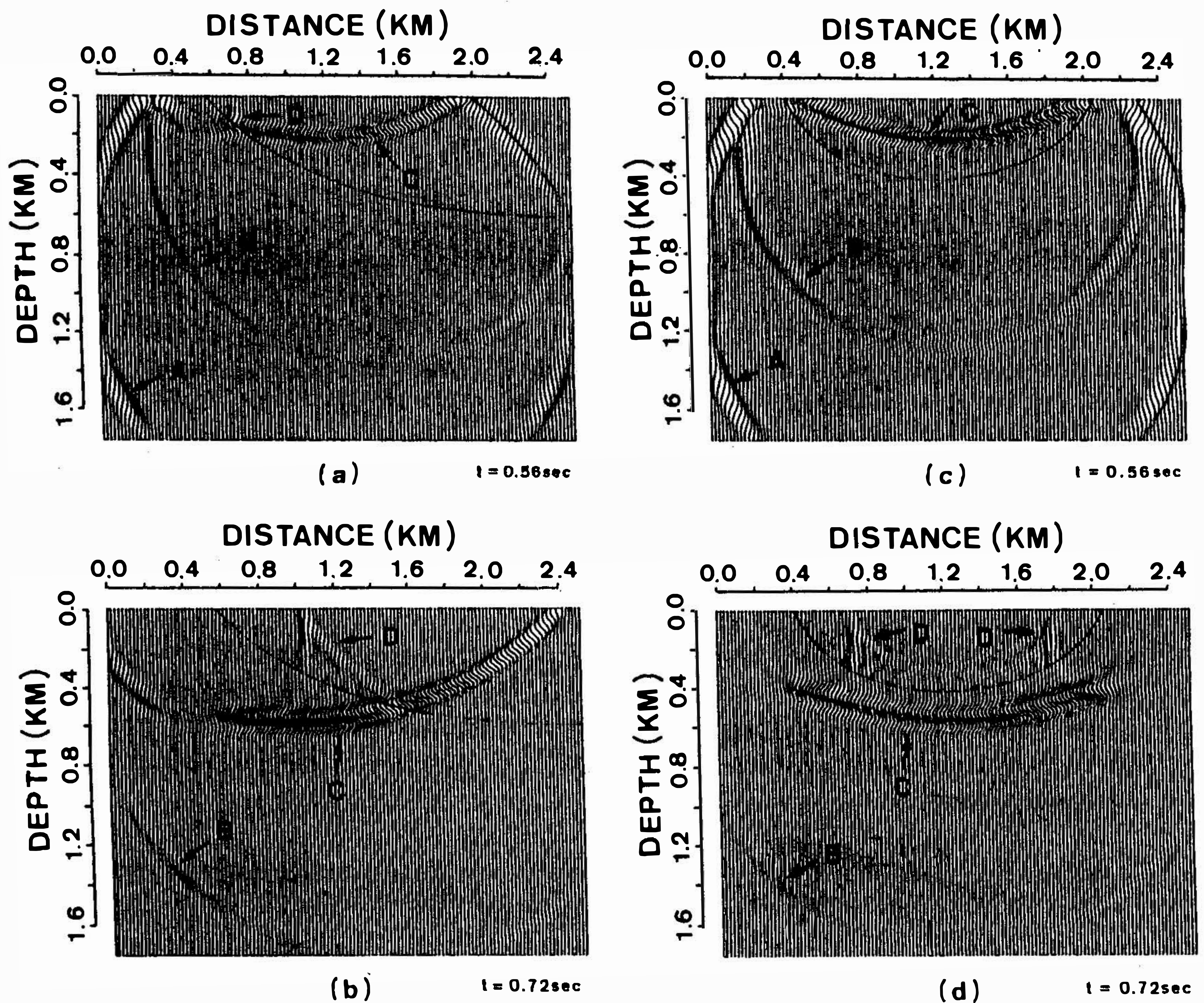
Fig. 14. 2-D wavefield snapshots for cross-sections of the 3-D sediment-filled basin model (Fig. 7) on (a) t=0.56 sec and (b) t=0.72 sec at y=1.2 km, and on (c) t=0.56 sec and (d) t=0.72 sec at x=1.3 km. The vertical axis is defined as the depth from free surface. The solid lines show the boundary of the basin and bedrock. Phase indexes refer to Fig. 9.

basin models and non-planar wavefronts generated by a point source. The focusing of the trapped wave energy and blocked-off wavefronts are clearly seen, and the resulting wavefield has a complex amplification pattern on the free surface. It has been found in this study that the low amplitude on rock sites at the basin edge, resulting from blocking off the incident wavefront by the basin cannot be reproduced by the plane wave incidence. In this case, the change of source location affects the path of incident wavefront through the interaction of wavefronts and the resulting amplitude.

In this study, a few cases have been tested, and only one typical case is chosen to demonstrate the 3-D basin effects. For a thorough exploration on 3-D wave propagation properties, rigorous computations on cases with different basin shapes and source locations are required. Ultimately, as in the acoustic case, one may derive elastic wave equations for the displacement field by following the above derivative procedure. However, the computation time and required storage memory are greatly increased in the elastic cases, limiting the

direct application of this method at this time. With the increased availability and speed of supercomputers, solutions to this computational problem will be overcome in the near future.

5. CONCLUSIONS

The numerical findings discussed above lead to the following conclusions:

(1) Consideration of the out-of-plane scattering of spherical wavefronts and calibration for apparent velocities is necessary when 2-D results are being applied to infer 3-D cases.

(2) The wavefront-blocking effect produced by the sediment-filled basin gives rise to low shacking amplitudes which cannot be reproduced by a model with a plane wave incidence.

(3) A basin trapped wave energy is found to propagate inwardly and focus near the center or the elliptical foci of the basin. This trapped wavefield is examined in different vertical cross-sections and time steps. The basin trends to trap the wave energy inside which results in much lengthened strong shacking motions. This trapped wave extends to the basin bottom with decreasing amplitude.

(4) Site effects are strongly affected by the point-source-generated spherical wavefronts which interact with the basin boundary, causing very complex strong shacking patterns through wave focusing. This focusing and soft basin trapped wave energy essentially produce the large-amplitude and the long-duration strong ground shacking that usually inflicts severe damage to structures, such as in the case of the recent Northridge earthquake.

REFERENCES

Abrahamson, N. A., B. A. Bolt, R. B. Darragh, J. Penzien, and Y. B. Tsai, 1987: The SMART-1 accelerograph array (1980-1987): A review. *Earthquake Spectra*, 3, 263-287.

Aki, K., and K. L. Larner, 1970: Surface motion of a layered medium having an irregular interface due to incident plane SH waves. *J. Geophys. Res.*, 75, 933- 954.

Benz, H. M., and R. B. Smith, 1988: Elastic-wave propagation and site amplification in the Salt Lake Valley, Utah, from simulated normal faulting earthquakes. *Bull. Seism. Soc. Am.*, 78, 1851-1874.

Boore, D. M., 1972: Finite-difference methods for seismic wave propagation in heterogeneous materials. In: B. A. Bolt,(Ed.), Methods in computational physics, 11, Academic Press, Inc, 1-36.

Cerjan, C., D. Kosloff, R. Kosloff, and M. Reshef, 1985: A nonreflecting boundary condition for discrete acoustic and elastic wave equations. *Geophysics*, 50, 705-708.

Cerveny, V., M. M., Popov, and I. Psencik, 1982: Computation of wave fields in inhomogeneous media-Gaussian beam approach. *Geophys. J. R. Astr. Soc.*, **70**, 109-128.

Daudt, C. R., L. W. Braile, R. L. Nowack, and C. S. Chiang, 1989: A comparison of finite-difference and Fourier method calculations of synthetic seismograms. *Bull. Seism. Soc. Am.*, **79**, 1210-1230.

Dong, Z., and G. A. McMechan, 1991: Numerical modeling of seismic waves with a 3-D, anisotropic scalar-wave equation. *Bull. Seism. Soc. Am.*, **81**, 769-780.

Dravinski, M., 1983: Scattering of plane harmonic SH wave by dipping layers or arbitrary shape. *Bull. Seism. Soc. Am.*, **73**, 1303-1319.

Frankel, A., and J. Vidale, 1992: A three-dimensional simulation of seismic waves in the Santa Clara Valley, California, from a Loma Prieta aftershock. *Bull. Seism. Soc. Am.*, **82**, 2045-2074.

Frankel, A., 1993: Three-dimensional simulations of ground motions in the San Bernardino Valley, California, for hypothetical earthquakes on the San Andreas fault. *Bull. Seism. Soc. Am.*, **83**, 1020-1041.

Fornberg, B., 1987: The pseudospectral method, Comparisons with finite differences for the elastic wave equation. *Geophysics*, **52**, 483-501.

Gazdag, J., 1973: Numerical convective schemes based on the accurate computation of space derivatives. *J. Comp. Phys.*, **13**, 100-113.

Gazdag, J., 1981: Modeling of the acoustic wave equation with transform methods. *Geophysics*, **46**, 854-859.

Hong, T. L., and D. V. Helmberger, 1978: Glorified optics and wave propagation in nonplanar structure. *Bull. Seism. Soc. Am.*, **68**, 2013-2032.

Huang, B. S., and Y. T. Yeh, 1991: Numerical modeling of wave propagation effects by the pseudo-spectrum method. *Proc. 3rd Taiwan Symposium Geophysics*, Chungli, 34-46.

Huang, B. S., 1992: A program for two-dimensional seismic wave propagation by the pseudo-spectrum method. *Computers and Geosciences*, **18**, 289-307.

Johnson, O. G., 1984: Three-dimensional wave equation computations on vector computers. *Proc. IEEE*, **72**, 90-95.

Khair, K. R., S. K. Datta, and A. H. Shah, 1989: Amplification of obliquely incident seismic waves by cylindrical alluvial valleys of arbitrary cross-sectional shape. *Bull. Seism. Soc. Am.*, **79**, 610-630.

Kosloff, D., and E. Baysal, 1982: Forward modeling by a Fourier method. *Geophysics*, **47**, 1402-1412.

Kosloff, D., M. Reshef, and D. Loewenthal, 1984: Elastic wave calculations by the Fourier method. *Bull. Seism. Soc. Am.*, **74**, 875-891.

Mossessian, M., and M. Dravinski, 1990: Amplification of elastic waves by a three dimensional valley. part 1: steady state response, *Earthq. Eng. Struct. Dyn.*, **19**, 667-680.

Ohori, M. Koketsv, and T. Minami, 1990: Seismic response analysis of sediment-filled valley due to incident plane waves by three-dimensional Aki-Larner method. *Bull. Earthq. Res. Inst. Univ. Tokyo*, **65**, 433-461.

Orszag, S. A., 1972: Comparison of pseudospectral and spectral approximation. *Stud. Appl. Math.*, **51**, 253-259.

Reshef, M., and D. Kosloff, 1985: Applications of elastic forward modeling to seismic interpretation. *Geophysics*, **50**, 1266-1272.

Reshef, M., D. Kosloff, M. Edwards, and C. Hsiung, 1988a: Three-dimensional acoustic modeling by the Fourier method. *Geophysics*, **53**, 1175-1183.

Reshef, M, D. Kosloff, M. Edwards, and C. Hsiung, 1988b: Three-dimensional elastic modeling by the Fourier method. *Geophysics*, **53**, 1184-1193.

Smith, W. D., 1975: The application of finite element analysis to body wave propagation problems. *Geophys. J. R. Astr. Soc.*, **42**, 747-768.

Sochacki, J., R. Kubichek, J. George, W. R. Fletcher, and S. Smithson, 1987: Absorbing boundary conditions and surface waves. *Geophysics*, **52**, 60-71.

Temperton, C., 1983: Self-sorting mixed-radix fast Fourier transforms. *J. Comp. Phys.*, **52**, 1-23.

Temperton, C., 1985: Implementation of a self-sorting in-place prime factor FFT algorithm. *J. Comp. Phys.*, **58**, 283-299.

Trifunac, M. D., 1971: Surface motion of a semi-cylindrical alluvial valley for incident plane SH waves. *Bull. Seism. Soc. Am.*, **61**, 1755-1770.

Van den Berg, A. P., 1988: A hybrid solution for wave propagation problems in inhomogeneous media. In: N. J. Vlaar, G. Nolet, M. J. R. Wortel and S. A. P. L. Cloetingh, (Eds.), Mathematical Geophysics, 85-116, D. Reidel Publishing Company.

Wang, H. L., and M. D. Trifunac, 1974: Surface motion of a semi-elliptical alluvial valley for incident plane SH waves. *Bull. Seism. Soc. Am.*, **64**, 1389-1408.

Wen, K. L., T. C. Shin, H. Y. Peng, and K. S. Liu, 1994: Preliminary analysis of site responses in the Taipei basin. Proc. Fifth. Taiwan Symposium Geophysics, Chungli, 85-96.

Wylie, C. R., 1975: Advanced Engineering Mathematics. McGraw-Hill, Inc, 937pp.

Yomogida, K., and J. T. Etgen, 1993: 3-D wave propagation in the Los Angeles Basin for the Whittier-Narrows earthquake. *Bull. Seism. Soc. Am.*, **93**, 1325-1344.